

Basin-scale transport of hydrothermal dissolved metals across the South Pacific Ocean

Joseph A. Resing¹, Peter N. Sedwick², Christopher R. German³, William J. Jenkins³, James W. Moffett⁴, Bettina M. Sohst² & Alessandro Tagliabue⁵

Hydrothermal venting along mid-ocean ridges exerts an important control on the chemical composition of sea water by serving as a major source or sink for a number of trace elements in the ocean^{1–3}. Of these, iron has received considerable attention because of its role as an essential and often limiting nutrient for primary production in regions of the ocean that are of critical importance for the global carbon cycle⁴. It has been thought that most of the dissolved iron discharged by hydrothermal vents is lost from solution close to ridge-axis sources^{2,5} and is thus of limited importance for ocean biogeochemistry⁶. This long-standing view is challenged by recent studies which suggest that stabilization of hydrothermal dissolved iron may facilitate its long-range oceanic transport^{7–10}. Such transport has been subsequently inferred from spatially limited oceanographic observations^{11–13}. Here we report data from the US GEOTRACES Eastern Pacific Zonal Transect (EPZT) that demonstrate lateral transport of hydrothermal dissolved iron, manganese, and aluminium from the southern East Pacific Rise (SEPR) several thousand kilometres westward across the South Pacific Ocean. Dissolved iron exhibits nearly conservative (that is, no loss from solution during transport and mixing) behaviour in this hydrothermal plume, implying a greater longevity in the deep ocean than previously assumed^{6,14}. Based on our observations, we estimate a global hydrothermal dissolved iron input of three to four gigamoles per year to the ocean interior, which is more than fourfold higher than previous estimates^{7,11,14}. Complementary simulations with a global-scale ocean biogeochemical model suggest that the observed transport of hydrothermal dissolved iron requires some means of physicochemical stabilization and indicate that hydrothermally derived iron sustains a large fraction of Southern Ocean export production.

Hydrothermal fluids are enriched in iron (Fe) and manganese (Mn) by more than 10^6 relative to ambient deep ocean concentrations¹, and corresponding gross hydrothermal fluxes to the oceans are probably greater than those from global riverine inputs³. However, it has been well documented that most of the hydrothermal Fe is lost from the dissolved phase in the vicinity of ridge-axis vents, where hot ($\sim 350^\circ\text{C}$), acidic, anoxic hydrothermal fluids ascend and mix with cold, alkaline, oxic sea water, resulting in the formation of Fe-sulphides and/or Fe-oxyhydroxides^{2,5}, which are subsequently lost from solution owing to settling and scavenging. As a result of these removal processes, it has been widely assumed that seafloor hydrothermal emissions are not a major source of dissolved Fe (Fe_d) to the ocean⁶. In contrast, dissolved Mn (Mn_d) is oxidized more slowly than Fe_d in sea water, and hydrothermal Mn_d anomalies have been observed as far as 2,000 km from ridge-axis sources¹⁵.

A number of recent studies have demonstrated that Fe_d can be stabilized against precipitation, aggregation, and scavenging losses

from sea water by several different physicochemical mechanisms^{7–10}. Such findings imply that hydrothermal activity could strongly affect the oceanic Fe_d inventory; however, comprehensive observational data on the persistence and fate of hydrothermal Fe are needed to evaluate this hypothesis. Although several recent studies have inferred the transport of hydrothermal Fe_d over distances of hundreds^{16,17} to thousands of kilometres^{11–13}, those conclusions remain equivocal at the ocean basin-scale, owing to limited sampling coverage^{11–13} and assumptions regarding synoptic distributions of the hydrothermal tracer helium-3 (${}^3\text{He}$)^{11,13,16}.

Here we present data for samples collected from 35 hydrographic stations between Manta, Ecuador, and Papeete, Tahiti, during the US GEOTRACES Eastern Pacific Zonal Transect (GEOTRACES cruise GP16; Fig. 1). This expedition focused on the Peru upwelling region and the superfast-spreading southern East Pacific Rise (SEPR), one of the most volcanically active areas on Earth and the source of a well documented plume of hydrothermal ${}^3\text{He}$ that extends west across the deep South Pacific Ocean¹⁸. The data from this cruise reveal pronounced gradients in Fe_d , Mn_d , dissolved aluminium (Al_d), and excess ${}^3\text{He}$ (${}^3\text{He}_{xs}$) concentrations along the $\sim 8,000$ -km-long cruise transect (Fig. 2).

The most striking and novel feature that we observed is a vast, mid-depth plume of elevated Fe_d and Mn_d that extends over a distance of more than 4,000 km to the west of the SEPR. This plume is carried by the westward-flowing mid-depth circulation^{18–20}, and is clearly defined by anomalous concentrations of ${}^3\text{He}_{xs}$ (Fig. 2). The distance over which Fe_d and Mn_d are transported from the SEPR is substantially greater than that observed in plumes identified from basin-scale sections across the Atlantic, Indian, Arctic, and Southern oceans^{12,16,17,21–23}. Also notable are the elevated Al_d concentrations that extend more than 3,000 km west of the SEPR; enrichments of this magnitude and extent have not

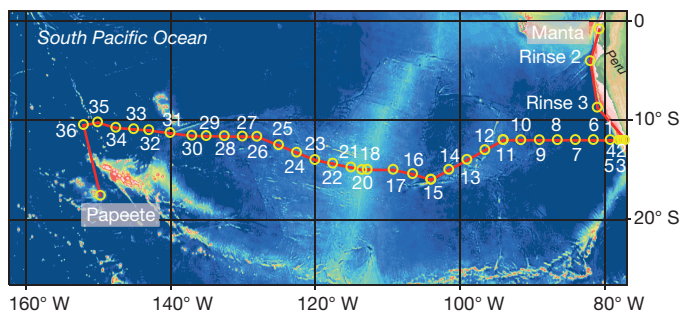


Figure 1 | Cruise track and station locations. The US GEOTRACES Eastern Pacific Zonal Transect (GEOTRACES cruise GP16) was undertaken on RV *Thomas G. Thompson* cruise 303 from 25 October to 20 December 2013. Station locations are shown as yellow circles with station numbers in white. Station 18 is located over the crest of the East Pacific Rise.

¹Joint Institute for the Study of the Atmosphere and the Ocean, University of Washington and NOAA-PMEL, 7600 Sand Point Way NE, Seattle, Washington 98115, USA. ²Department of Ocean, Earth and Atmospheric Sciences, Old Dominion University, Norfolk, Virginia 23529, USA. ³Woods Hole Oceanographic Institution, Woods Hole, Massachusetts 02543, USA. ⁴Department of Biological Sciences, University of Southern California, 3616 Trousdale Parkway #AHF204, Los Angeles, California 90089, USA. ⁵Department of Earth, Ocean and Ecological Sciences, School of Environmental Sciences, University of Liverpool, 4 Brownlow Street, Liverpool L69 3GP, UK.

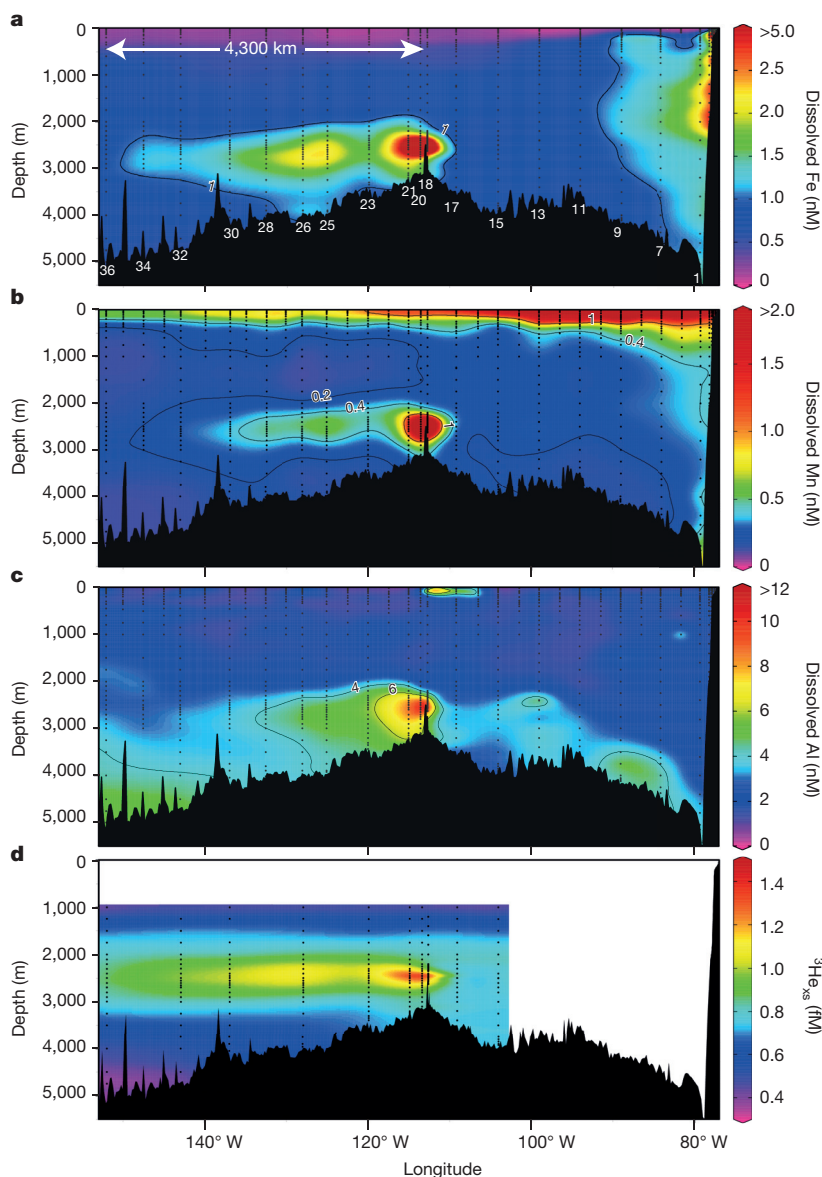


Figure 2 | Interpolated zonal concentration for GEOTRACES Eastern Pacific Zonal Transect.
a, Dissolved iron. **b**, Dissolved manganese.
c, Dissolved aluminium. **d**, Excess helium-3 (${}^3\text{He}_{\text{xs}}$). Station numbers and distance west of East Pacific Rise are indicated on uppermost panel.

been previously reported for hydrothermal plumes in the Pacific, Arctic, Southern, or Indian oceans^{12,21,22,24,25} (see also the GEOTRACES Intermediate Data Product, <http://www.bodc.ac.uk/geotrades/data/idp2014/>). Given the differences in geochemical behaviour between Fe and Mn, it is surprising that the lateral extent of the hydrothermal Fe_d anomaly exceeds that of Mn_d ; inventories of hydrothermal Fe_d and Mn_d (Fe_d and Mn_d minus background) at station 32 are $\sim 11\%$ and $\sim 4\%$, respectively, of those at station 20 (see Fig. 1). Our data set clearly documents the long-range transport of hydrothermal Fe_d from the SEPR, thus confirming the tentative conclusions drawn from limited previous observations^{11,13}.

Directly over the SEPR at station 18, Fe_d in the ‘near field’ hydrothermal plume is only $\sim 20\%$ of the total dissolvable Fe (an approximate measure of total hydrothermal Fe), and $\text{Fe}(\text{II})$ concentrations are near background levels. This suggests rapid oxidation and loss of hydrothermal Fe from the dissolved phase close to the ridge axis, consistent with previous observations from the SEPR⁵. In contrast, from the first off-axis station (station 20) continuing west across the basin as far as station 36, Fe_d concentrations are linearly correlated with ${}^3\text{He}_{\text{xs}}$ within the plume (Fig. 3a, b and Extended Data Fig. 1), indicating that hydrothermal Fe_d is behaving conservatively and therefore decreases in its concentration (as for the inert ${}^3\text{He}_{\text{xs}}$) reflect only mixing and dilution over a distance of $\sim 4,300$ km. Such behaviour is unexpected, given the

known propensity for the oxidation, aggregation, and scavenging of Fe_d from sea water^{2,4,5}. Accordingly, our observations imply that Fe_d in the hydrothermal plume is somehow stabilized against loss from solution, perhaps as a result of complexation by dissolved organic ligands^{7,8}, or by incorporation into inorganic or organic colloids that reside within the dissolved ($<0.2\ \mu\text{m}$) size fraction^{9,10}.

The relationship between Mn_d and ${}^3\text{He}_{\text{xs}}$ in the plume (Fig. 3c, d) indicates that hydrothermal Mn is removed from the dissolved phase until it reaches station 21, beyond which the residual hydrothermal Mn_d , like Fe_d , behaves conservatively with respect to ${}^3\text{He}_{\text{xs}}$. Dissolved Al over the ridge crest is enriched by as much as 12 nM over mid-depth concentrations to the east of the SEPR. This is comparable to enrichments in hydrothermal plumes over the Mid-Atlantic Ridge^{23,26}, where Al-rich plumes are spatially restricted to the deep axial valley and are thought to reflect the entrainment of Al-rich waters by rising hydrothermal fluids during plume formation²⁶. In contrast, the SEPR typically lacks an axial valley, and the Al_d plume extends far from the ridge crest, suggesting a larger source of Al_d along the SEPR. Dissolved Al concentrations exceeding 100 nM have been reported in unusually acidic hydrothermal plumes that may be associated with seafloor eruptive activity²⁷, and the SEPR between 14°S and 19°S is a particularly active locus of seafloor volcanism, with hydrothermal and eruptive activity being more intense than along most other ridge sec-

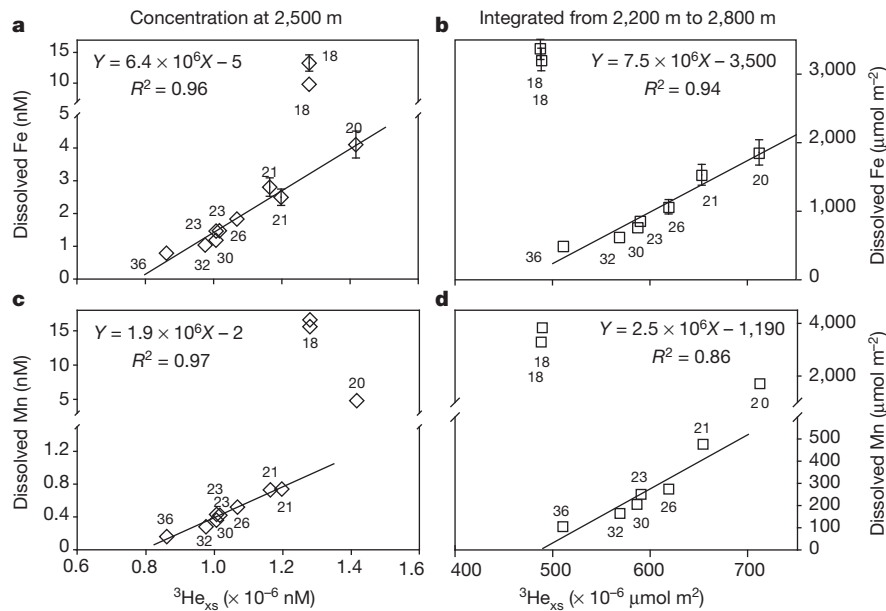


Figure 3 | Relationship between dissolved trace metals and ${}^3\text{He}$ west of SEPR. **a**, Dissolved iron versus ${}^3\text{He}_{\text{xs}}$ at 2,500 m depth ($n = 11$). **b**, Dissolved Fe versus ${}^3\text{He}_{\text{xs}}$, both integrated over a depth of 2,200–2,800 m except at station 18, where the maximum depth was 2,640 m ($n = 9$). **c**, Dissolved manganese versus ${}^3\text{He}_{\text{xs}}$ at a depth of 2,500 m ($n = 11$). **d**, Dissolved manganese versus ${}^3\text{He}_{\text{xs}}$ integrated as in **b** ($n = 9$). Error bars are twice the relative standard deviation of a given analysis, as reported in the Methods. Error bars are absent where the symbol size exceeds the error estimate. Lines represent the slope of a

tions worldwide^{5,28}. This suggests that eruptive activity is one possible source of the SEPR Al_d plume.

We assess the importance of physicochemical stabilization to the long-range transport of hydrothermal Fe_d using numerical simulations of Fe_d and ${}^3\text{He}_{\text{xs}}$ within a global-scale ocean biogeochemical

simple linear regression analysis of the data. Discrete and integrated ${}^3\text{He}_{\text{xs}}$ concentrations are lower at station 18 relative to stations west of the ridge; this difference is reduced for integrations between 2,200 m and 2,640 m depth (Extended Data Fig. 1a). The relatively low ${}^3\text{He}_{\text{xs}}$ concentrations at station 18 ($\sim 15^\circ \text{S}$) suggest that the off-axis plume (stations 20–36) is primarily derived from vent fields located further south ($\sim 17^\circ \text{S}$ – 18.5°S) on the SEPR^{5,28} with hydrothermal and eruptive effluent being homogenized and transported north and west²⁰ by along-axis and off-axis transport processes^{20,30}.

model that includes explicit cycling of dissolved Fe-binding ligands (see Methods). The model represents the input of ${}^3\text{He}$ as a function of ridge spreading rate and simulates hydrothermal Fe efflux via a fixed Fe: ${}^3\text{He}$ ratio estimated from a global compilation of hydrothermal fluids¹⁴. Although there is reasonable qualitative agreement

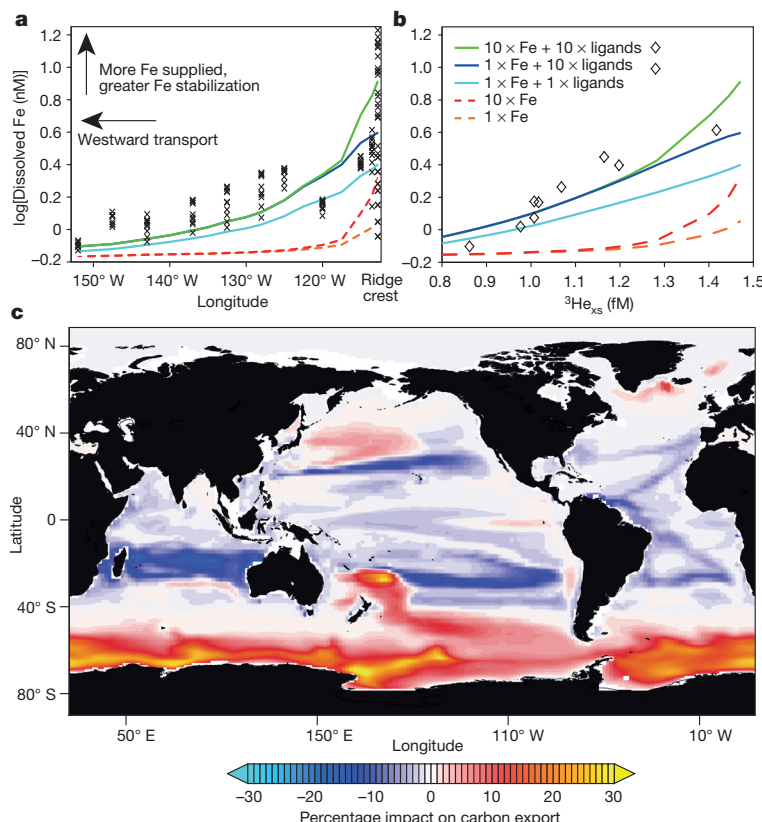


Figure 4 | Results of biogeochemical model simulations. Model simulation results centred at 2,530 m depth (average of two depth bins spanning 2,060–3,010 m; coloured lines) are shown in **a** and **b**. **a**, Dissolved Fe from model results compared to measured Fe_d concentrations (crosses) between 2,200 m and 2,800 m to the west of the ridge axis. **b**, Dissolved Fe versus ${}^3\text{He}_{\text{xs}}$ from model simulations compared to measured values (diamonds) at 2,500 m depth. For **a** and **b** the individual model simulations were run for 75 years. Orange dashed line, model solution using base hydrothermal Fe flux ($1 \times \text{Fe}$). Red dashed line, $10 \times$ base hydrothermal Fe flux ($10 \times \text{Fe}$). Cyan line, base hydrothermal Fe flux with equimolar flux of ligands ($1 \times \text{Fe} + 1 \times \text{ligands}$). Dark blue line, base hydrothermal Fe flux with $10 \times$ greater ligand flux ($1 \times \text{Fe} + 10 \times \text{ligands}$). Green line, $10 \times$ base Fe flux with equimolar flux of ligands ($10 \times \text{Fe} + 10 \times \text{ligands}$). **c**, Percentage of annual export production due to hydrothermal Fe based on a 500-year model simulation employing base hydrothermal Fe flux with equimolar ligand flux ($1 \times \text{Fe} + 1 \times \text{ligands}$) relative to a model solution with no hydrothermal Fe or ligand flux. Lower export production in the subtropical oceans is caused by decreased preformed macronutrients in the mode waters.

with our $^3\text{He}_{\text{xs}}$ data (Extended Data Fig. 2), the sluggish deep-ocean circulation typical of relatively coarse-resolution global models restricts the overall westward transport of the hydrothermal anomaly (a feature that has proved challenging to measure and model^{19,20}).

Even allowing for this insufficient abyssal propagation, Fe_d concentrations and their relation to $^3\text{He}_{\text{xs}}$ decrease rapidly to the west of the ridge crest owing to scavenging, when only hydrothermal Fe input is considered (Fig. 4a, b and Extended Data Fig. 3a); a tenfold increase in Fe input results in no improvement in the agreement with observations (Fig. 4a, b and Extended Data Fig. 3b). In contrast, when dissolved Fe-stabilizing ‘ligands’ from vent fluids or from processes occurring within the plume are added in an equimolar ratio with hydrothermal Fe_d , a much greater westward propagation of the Fe_d plume is achieved and the model is better able to reproduce both the plume extent and relationship between Fe_d and $^3\text{He}_{\text{xs}}$ (Fig. 4a, b and Extended Data Fig. 3c–e). Adding tenfold more ligands, or tenfold more ligands and tenfold more hydrothermal Fe further increases the plume extent (note the logarithmic scale in Fig. 4a and b). Importantly, including a hydrothermal supply of ligands also improves the degree to which the model can reproduce the global distributions of Fe_d in the abyssal ocean (Extended Data Table 1). A similar result would be expected for the formation of relatively unreactive Fe nanoparticles or colloids within the near-field plume^{9,10}, so the dissolved Fe-stabilizing ‘ligands’ could involve organic or inorganic moieties. These process-based model experiments indicate that the total input of hydrothermal Fe regulates the magnitude of the Fe_d plume near the ridge crest, whereas the stabilization of Fe_d against loss from solution governs its persistence and transport in the deep ocean.

Although recent global-scale models of the ocean Fe cycle suggest substantial hydrothermal contributions to the deep-ocean Fe inventory¹⁴, our data indicate that this previous work substantially underestimated the far-field influence of hydrothermal Fe_d emissions. The linear relationship between Fe_d and $^3\text{He}_{\text{xs}}$ concentrations in the plume west of the SEPR has a slope of $7.5 \pm 0.8 \times 10^6$ moles Fe_d per mole $^3\text{He}_{\text{xs}}$ (s.d. of slope based on simple linear regression; Fig. 3b), which falls roughly midway between values estimated for hydrothermal plumes in the western South Pacific, the Southern Ocean, and the South Atlantic^{11,14,16}. If this relationship is representative of steady-state mid-ocean-ridge hydrothermal inputs to the ocean, then the estimated global hydrothermal ^3He efflux of 530 mol yr^{-1} (ref. 29) yields an ‘effective’ hydrothermal Fe_d input of about $4 \pm 1 \text{ Gmol yr}^{-1}$ to the ocean interior, which is at least fourfold higher than previous estimates^{7,11,14}. This Fe_d is ultimately supplied to the iron-deficient surface waters of the Southern Ocean, where it supports $\sim 15\%$ to 30% of the modelled export production south of the Polar Front (Fig. 4c). The impact of hydrothermal Fe on export production is driven both by its gross flux and by processes that govern its stabilization (Extended Data Fig. 4). Thus, the ultimate impacts of hydrothermal activity on the biogeochemical cycle of Fe in the ocean may depend as much on the processes that control the longevity of hydrothermal Fe_d plumes as on the magnitude of the hydrothermal Fe emissions, on which prior studies have largely focused.

Online Content Methods, along with any additional Extended Data display items and Source Data, are available in the online version of the paper; references unique to these sections appear only in the online paper.

Received 9 January; accepted 14 May 2015.

- Von Damm, K. L. Seafloor hydrothermal activity: black smoker chemistry and chimneys. *Annu. Rev. Earth Planet. Sci.* **18**, 173–204 (1990).
- German, C. R. & Seyfried, W. E. in *Treatise Geochemistry* Vol. 8 (eds Holland, H. D. & Turekian, K. K.) 191–233 (Elsevier, 2014).
- Elderfield, H. & Schultz, A. Mid-ocean ridge hydrothermal fluxes and the chemical composition of the ocean. *Annu. Rev. Earth Planet. Sci.* **24**, 191–224 (1996).
- Boyd, P. W. & Ellwood, M. J. The biogeochemical cycle of iron in the ocean. *Nature Geosci.* **3**, 675–682 (2010).
- Feeley, R. A. et al. Hydrothermal plume particles and dissolved phosphate over the superfast-spreading southern East Pacific Rise. *Geochim. Cosmochim. Acta* **60**, 2297–2323 (1996).
- Burland, K. & Lohan, M. in *Treatise Geochemistry* Vol. 6 (eds Holland, H. D. & Turekian, K. K.) 23–47 (Elsevier, 2003).
- Bennett, S. A. et al. The distribution and stabilisation of dissolved Fe in deep-sea hydrothermal plumes. *Earth Planet. Sci. Lett.* **270**, 157–167 (2008).
- Sander, S. G. & Koschinsky, A. Metal flux from hydrothermal vents increased by organic complexation. *Nature Geosci.* **4**, 145–150 (2011).
- Yücel, M., Gartman, A., Chan, C. S. & Luther, G. W. Hydrothermal vents as a kinetically stable source of iron-sulphide-bearing nanoparticles to the ocean. *Nature Geosci.* **4**, 367–371 (2011).
- Sands, C. M., Connolly, D. P., Statham, P. J. & German, C. R. Size fractionation of trace metals in the Edmond hydrothermal plume, Central Indian Ocean. *Earth Planet. Sci. Lett.* **319–320**, 15–22 (2012).
- Fitzsimmons, J. N., Boyle, E. A. & Jenkins, W. J. Distal transport of dissolved hydrothermal iron in the deep South Pacific Ocean. *Proc. Natl. Acad. Sci. USA* **111**, 16654–16661 (2014).
- Nishioka, J., Obata, H. & Tsumune, D. Evidence of an extensive spread of hydrothermal dissolved iron in the Indian Ocean. *Earth Planet. Sci. Lett.* **361**, 26–33 (2013).
- Wu, J., Wells, M. L. & Rember, R. Dissolved iron anomaly in the deep tropical-subtropical Pacific: evidence for long-range transport of hydrothermal iron. *Geochim. Cosmochim. Acta* **75**, 460–468 (2011).
- Tagliabue, A. et al. Hydrothermal contribution to the oceanic dissolved iron inventory. *Nature Geosci.* **3**, 252–256 (2010).
- Klinkhammer, G. & Hudson, A. Dispersal patterns for hydrothermal plumes in the South Pacific using manganese as a tracer. *Earth Planet. Sci. Lett.* **79**, 241–249 (1986).
- Saito, M. A. et al. Slow-spreading submarine ridges in the South Atlantic as a significant oceanic iron source. *Nature Geosci.* **6**, 775–779 (2013).
- Conway, T. M. & John, S. G. Quantification of dissolved iron sources to the North Atlantic Ocean. *Nature* **511**, 212–215 (2014).
- Lupton, J. & Craig, H. A major helium-3 source at 15°S on the East Pacific Rise. *Science* **214**, 13–18 (1981).
- Talley, L. & Johnson, G. Deep, zonal subequatorial currents. *Science* **263**, 1125–1128 (1994).
- Hautala, S. & Riser, S. A nonconservative β -spiral determination of the deep circulation in the eastern South Pacific. *J. Phys. Oceanogr.* **23**, 1975–2000 (1993).
- Middag, R., de Baar, H. J. W., Laan, P. & Bakker, K. Dissolved aluminium and the silicon cycle in the Arctic Ocean. *Mar. Chem.* **115**, 176–195 (2009).
- Middag, R., van Slooten, C., de Baar, H. J. W. & Laan, P. Dissolved aluminium in the Southern Ocean. *Deep Sea Res. II* **58**, 2647–2660 (2011).
- Measures, C., Hatta, M., Fitzsimmons, J. & Morton, P. Dissolved Al in the zonal N Atlantic section of the US GEOTRACES 2010/2011 cruises and the importance of Hydrothermal inputs. *Deep-Sea Res. II* **116**, 176–186 (2015).
- Lupton, J. E. et al. Chemical and physical diversity of hydrothermal plumes along the East Pacific Rise, 8°45' N to 11°50' N. *Geophys. Res. Lett.* **20**, 2913–2916 (1993).
- Klunder, M. B., Laan, P., Middag, R., de Baar, H. J. W. & van Ooijen, J. C. Dissolved iron in the Southern Ocean (Atlantic sector). *Deep Sea Res. II* **58**, 2678–2694 (2011).
- Lunel, T., Rudnicki, M., Elderfield, H. & Hydes, D. Aluminium as a depth-sensitive tracer of entrainment in submarine hydrothermal plumes. *Nature* **344**, 137–139 (1990).
- Gamo, T. et al. Hydrothermal plumes in the eastern Manus Basin, Bismarck Sea: CH_4 , Mn, Al and pH anomalies. *Deep Sea Res. I* **40**, 2335–2349 (1993).
- Urabe, T. et al. The effect of magmatic activity on hydrothermal venting along the superfast-spreading East Pacific Rise. *Science* **269**, 1092–1095 (1995).
- Farley, K., Maier-Reimer, E., Schlosser, P. & Broeker, W. S. Constraints on mantle ^3He fluxes and deep-sea circulation from an oceanic general circulation model. *J. Geophys. Res.* **100**, 3829–3839 (1995).
- Thurnherr, A. M., Ledwell, J. R., Lavelle, J. W. & Mullineaux, L. S. Hydrography and circulation near the crest of the East Pacific Rise between 9° and 10°N. *Deep. Sea Res. I* **58**, 365–376 (2011).

Acknowledgements We thank the captain and crew of the RV *Thomas G. Thompson* (TGT cruise 303) for their support during the 57-day mission. Samples were collected on board ship by C. Parker and C. Zurbrock, from the US GEOTRACES sampling system maintained and operated by G. Cutter. We thank the many people who have devoted time and effort to the international GEOTRACES programme. This work was funded by US National Science Foundation awards OCE-1237011 to J.A.R., OCE-1237034 to P.N.S., OCE-1232991 to W.J.J., OCE-1130870 to C.R.G., and OCE-1131731 and OCE-1260273 to J.W.M. Model simulations made use of the N8 HPC facilities, funded by the N8 consortium and EPSRC grant EP/K00225/1. C.R.G. also acknowledges support from a Humboldt Research Award. J.A.R. was funded in part through JISAO by the PMEL-Earth Oceans Interactions programme. This is JISAO publication number 2388 and PMEL publication number 4255.

Author Contributions J.A.R. participated on the EPZT and determined Al_d and Mn_d ; P.N.S. interpreted the Fe_d data; C.R.G. co-designed the study and participated in the EPZT; W.J.J. collected $^3\text{He}_{\text{xs}}$ data; J.W.M. co-designed the study, participated in the EPZT, and collected $\text{Fe}(d)$ data; B.M.S. participated in the EPZT and determined Fe_d ; A.T. conducted the modelling experiments and interpreted their results. All authors contributed to the writing of the manuscript.

Author Information Reprints and permissions information is available at www.nature.com/reprints. The authors declare no competing financial interests. Readers are welcome to comment on the online version of the paper. Correspondence and requests for materials should be addressed to J.A.R. (resing@uw.edu) or A.T. (a.tagliabue@liverpool.ac.uk, for code).

METHODS

Sample collection and processing. Water column samples for trace metal analyses were obtained using 24 modified 12-litre GO-FLO bottles (General Oceanics) mounted on a trace-metal-clean conductivity–temperature–depth carousel (SeaBird) that was deployed on a Kevlar conducting cable³¹. Upon recovery, the GO-FLO samplers were brought into a shipboard Class-100 clean laboratory container for sub-sampling. For filtered samples, the samplers were pressurized to 10 psi using filtered, compressed air, and the seawater samples were filtered through pre-cleaned 0.2-μm Acropak Supor capsule filters (Pall) using rigorous trace-metal-clean protocols³¹. The Eastern Pacific Zonal Transect (EPZT) occupied 35 sampling stations along more than 8,000 km of cruise track. At 17 stations denoted as ‘full’ or ‘super’ stations, 37 samples were collected between the surface and the sea floor; at one additional station (station 34), 25 samples were collected over the upper 3,000 m of the water column. At 13 stations, denoted ‘demi’ stations, 13 samples were collected in the upper 1,000 m; and at 4 stations over the continental shelf, 7–24 samples were collected between the surface and sea floor. For Mn_d and Al_d, 876 samples were collected from all stations and depths. The 0.2-μm filtered subsamples were stored in 100-ml low-density polyethylene (LDPE) bottles (Bel-Art) with LDPE caps and were acidified to pH ≈ 1.7 with 12 N ultrapure hydrochloric acid (Fisher Optima). For Fe_d, 760 samples were collected at the full and super stations, with 0.2-μm filtered subsamples stored in 125-ml LDPE bottles with polypropylene caps (Nalgene) and acidified to pH ≈ 1.7 with a 6 N solution of ultrapure hydrochloric acid (Fisher Optima). Unfiltered seawater samples for the analysis of total dissolvable iron and manganese were collected at all full stations west of 109° W from the 24 deepest samples. These samples were collected in 125-ml LDPE bottles with polypropylene caps (Nalgene) and acidified to pH ≈ 1.7 with 12 N ultrapure hydrochloric acid (Fisher Optima), then stored for >4 months before analysis. Sample collection for Fe(II) analysis was identical to that for total dissolved metals, with the exception that the seawater samples were drawn into acid-washed 50-ml AirTite All-Plastic Norm-Ject syringes (Fisher Scientific) in the GEOTRACES sampling van to exclude oxygen contamination. These samples were stored on ice and in darkness to slow oxidation before analysis. Comparison with samples where Fe(II) was stabilized using 3-(N-morpholino)-propansulfonic acid buffer³² indicated that Fe(II) was effectively preserved using the syringe protocol. Independent measurements of Fe_d indicated no detectable contamination from the syringes. Seawater samples for dissolved helium analysis (~45 g each) were drawn from the standard rosette (12-position, 30-litre Niskin-type bottles) using Tygon tubing connected to lengths of 5/8" soft copper refrigeration tubing. Sample tubes were then hydraulically crimp-sealed³³.

Analytical methods. Dissolved Fe was determined at sea or at Old Dominion University by flow injection analysis with in-line pre-concentration on resin-immobilized 8-hydroxyquinoline and colorimetric detection^{34,35}, using a method modified from ref. 36. For the lowest-concentration samples from each analysis, and for SAFe seawater reference material S, the method of standard additions was used; all other samples were quantified using a standard curve obtained by addition of Fe standard solution to low-Fe sea water. For the cruise period, we determined the following Fe_d concentrations for the SAFe seawater reference materials: 0.126 ± 0.023 nM (*n* = 4) for SAFe seawater reference material S, and 1.26 ± 0.20 nM (*n* = 10) for SAFe seawater reference material D2. These values compare well with community consensus concentrations of 0.095 ± 0.008 nM and 0.955 ± 0.024 nM, respectively. In an effort to correct for day-to-day variations in analytical accuracy, all daily analyses included analysis of the GEOTRACES reference sea water, GSP, for which there is currently no consensus Fe_d concentration; all daily sample determinations were corrected using the difference between each day’s measured GSP concentration and the overall cruise average Fe_d concentration for the GSP seawater (0.34 ± 0.07 nM, *n* = 27). The analytical limit of detection is estimated as the Fe_d concentration equivalent to a peak area that is three times the standard deviation on the ‘zero-loading blank’ (‘manifold blank’), from which we estimate a detection limit of less than 0.04 nM^{34,37}. Blank contributions from the ammonium acetate sample buffer solution (added on-line during analysis) and hydrochloric acid (added after collection) are negligible (that is, too low to quantify). Robust estimates of analytical precision are derived from multiple separate determinations of the SAFe seawater reference materials, which yield analytical uncertainties (expressed as one relative sample standard deviation on the mean) of ~15% at the concentration level of SAFe S (~0.1 nM) and ~10% at the concentration level of SAFe D2 (~1 nM). For high Fe (>5 nM) samples, Fe was determined by modifying the flow injection method to include a sample loop, rather than a pre-concentration column, and by using deionized water acidified to pH ≈ 1.7 as a carrier in place of the acid eluent. This modified flow injection method had an analytical precision of ±4% or ±1.5 nM (whichever is greater). Suitable seawater reference materials were not available for these analyses.

Dissolved Mn was determined at sea by flow injection analysis with in-line pre-concentration on resin-immobilized 8-hydroxyquinoline and colorimetric

detection³⁸. Daily precision of analysis was ±0.01 nM (one standard deviation) or 3.8%, whichever is larger, based on the reproducibility of analytical and internal standards. A conservative estimate of the limit of detection is 0.03 nM based on three times the daily precision of analysis, which is consistent with previous work³⁸. Two internal reference standards were run over the 57 days of the cruise, with Mn_d concentrations of 0.42 ± 0.036 nM (±8.4%; *n* = 102) and 0.31 ± 0.041 nM (±13%, *n* = 69), respectively. The SAFe reference samples were analysed simultaneously during sample analysis with the following results: for SAFe S, 0.85 ± 0.026 nM (*n* = 27; consensus value 0.79 ± 0.06 nM); for SAFe D2, 0.40 ± 0.028 nM (*n* = 22; consensus value 0.35 ± 0.05); and for SAFe D1, 0.36 ± 0.026 nM (*n* = 31; no consensus value). Analytical uncertainty is expressed as ± one standard deviation.

Dissolved Al was determined at sea by flow injection analysis with in-line pre-concentration and fluorimetric detection³⁹. Method modifications included replacing resin-immobilized 8-hydroxyquinoline with Toyopearl AF-Chelate 650M, and using acidified de-ionized water as the carrier instead of acidified seawater. Daily precision for repeat analysis of internal and primary standards was ±0.1 nM or 4.2%, whichever is larger. Two internal reference standards were run during the cruise, with Al_d concentrations of 1.76 ± 0.25 nM (±14%; *n* = 101) and 1.98 ± 0.07 nM (±3.4%; *n* = 75), respectively. The SAFe reference samples were analysed simultaneously during sample analysis: for SAFe S, 2.38 ± 0.14 nM (*n* = 26; consensus value 1.67 ± 0.10 nM); for SAFe D2, 1.63 ± 0.13 nM (*n* = 26; consensus value 1.03 ± 0.09 nM); and for SAFe D1, 1.26 ± 0.11 nM (*n* = 32; consensus value 0.62 ± 0.03 nM). The least-squares best fit between our shipboard determinations and the SAFe consensus values is: Al_{shipboard} = 1.02Al_{SAFe} + 0.59 nM (*r*² = 0.99). Analytical uncertainty is expressed as ± one standard deviation. In the past, our laboratory has produced Al_d determinations that were statistically indistinguishable from the SAFe consensus concentrations, suggesting that our shipboard analytical method includes a consistent, unidentified blank equivalent to ~0.6 nM Al_d. Our estimated limit of detection of 0.3 nM based on daily precision estimates is low and might more conservatively be estimated to be >0.6 nM. The anomalously high Al_d concentrations (3.7–29.5 nM) determined in samples collected from 20–150 m depth at stations near 109° W and 113° W are not readily explained by ancillary chemical and physical data from the cruise, although there is no apparent reason to suspect that these few samples were contaminated during collection, processing, or analysis.

Fe(II) was determined at sea using an automated flow injection analysis system (FeLume II, Waterville Analytical) employing a Luminol chemiluminescence detection system^{32,40}. The FeLume system was fitted with a standard quartz flow cell and a Hamamatsu HC135 photon counter configured with the following settings: pump speed of 15 rpm; photon counter integration time of 200 ms; load time of 20 s. The mean of the last 50 data points was used to determine the signal. Detection limits were determined for surface samples where ferrous iron was negligible based on a standard 3σ evaluation of the baseline signal^{32,40}. This yielded an estimated detection limit of 14 pmol l⁻¹.

Helium was determined ashore after gases from the samples were quantitatively extracted under a vacuum into liquid-nitrogen chilled ~25-ml aluminosilicate glass flasks and sealed before analysis. Sample processing on the mass spectrometer system included purification over SAES getters to remove reactive gases and use of cryogenics to separate the noble gases^{41–43}. Sample integrity was evaluated using noble gas abundances (not reported here), and determined by quadrupole mass spectrometer with an accuracy of 0.1%–0.5%, depending on the gas. The helium abundance and isotope ratio (³He/⁴He) were determined using a branch-tube magnetic sector mass spectrometer to an accuracy of 0.15% or better as determined by reproducibility of standards and duplicate samples. The isotope ratio was referenced to an atmospheric standard. Excess ³He is computed as an approximate measure of the non-atmospheric ³He over saturation:

$$\delta^3\text{He}_{\text{xs}} = (\delta^3\text{He} - \delta^{3\text{He}})/100 \times C[\text{He}] \times 1.384 \times 10^{-6}$$

where $\delta^3\text{He} = 100 \times (R_{\text{x}}/R_{\text{a}} - 1) \times 100\%$, R_{x} and R_{a} are the ³He/⁴He ratios of the sample and air (1.384×10^{-6}), respectively. $\delta^{3\text{He}}$ is the helium isotope ratio anomaly in solubility equilibrium with the atmosphere, which is a weak function of temperature⁴⁴ and is about –1.8% for the data used here. The precision of $\delta^3\text{He}_{\text{xs}}$ is 0.5% at 1 fM. The precision of $\delta^3\text{He}_{\text{xs}}$ is more than tenfold better than that of either Fe_d or Mn_d, allowing the use of a type I linear regression when comparing Fe_d and Mn_d to $\delta^3\text{He}_{\text{xs}}$.

The PISCES biogeochemical model. The model employed in this study is currently the only global-scale version that considers hydrothermal input of iron and a dynamic representation of iron-binding ligands⁴⁵. The PISCES model^{46,47} is a relatively complex ocean general circulation and biogeochemistry model that includes two phytoplankton groups, two zooplankton grazers, five limiting nutrients (nitrate, phosphate, silicic acid, ammonium, and Fe) and two size classes of organic carbon particles, calcium carbonate and biogenic silica, which sink and are

remineralized differentially. Dissolved Fe is supplied to the ocean from dust, sediments, rivers, and hydrothermal vents⁴⁷ and is ultimately lost to the sediments. The Fe_d is subjected to scavenging/coagulation losses, which produce two size classes of particulate iron. The scavenging rate is computed in the model by calculating the amount of 'free' uncomplexed Fe_d (assuming a dynamic ligand concentration and conditional stability) and the resulting net rate of scavenging depends on the concentrations of each particle species. We also account for the loss of organically complexed colloidal iron via coagulation processes and consider contributions from turbulent and Brownian components. The colloidal fraction of Fe_d is calculated as a function of temperature, salinity, and pH^{48,49}. Ligand dynamics are represented assuming sources from phytoplankton or zooplankton exudation and organic matter degradation, and sinks associated with photochemical degradation, colloidal coagulation, and variable bacterial consumption, all on a reactivity continuum⁴⁵. The ligand stability constants vary according to: pKFe'L = 17.27–1565.7/TK, where TK is absolute temperature leading to pKFe'L of 11.5 at 0 °C and 11.9 at 20 °C⁴⁵. Phytoplankton Fe_d uptake is computed using a quota model, with overall growth limitation accounting for the Fe demand associated with photosynthesis, respiration, and nitrate uptake⁵⁰. PISCES is coupled to the three-dimensional ocean general circulation model NEMO, which has a spatial resolution of 2° of longitude, 2 × cos(latitude) that is enhanced to 0.5° at the Equator, and 31 vertical levels, with the first ten levels in the upper 100 m. Hydrothermal transport was mostly observed over vertical levels 25 (centred on 2,290 m, depth range 2,050–2,530 m) and 26 (centred on 2,770 m, depth range 2,530–3,010 m), which were used in Fig. 4a and b.

For this study we conducted a range of different simulations with PISCES aimed at addressing the processes responsible for the longevity of the observed hydrothermal Fe_d plume and their potential impact on the carbon cycle. The standard input flux of iron from the mid-ocean ridge was calculated based on iron-to-³He ratios in hydrothermal fluids and spreading rate¹⁴; note that the flux is not based on the Fe_d flux calculated here. First, we conducted a set of experimental simulations over 75 years (outlined in Fig. 4) to examine the plume extent. To assess the large-scale impact of hydrothermal Fe and 'hydrothermal ligands' on ocean biogeochemistry and productivity, we extended the run with the standard addition of hydrothermal Fe_d with ligands in a 1:1 molar ratio (1 × Fe + 1 × ligands) over a period of 500 years and compared that to a 500-year model run in which no hydrothermal Fe or ligands were added. After 500 years, the yearly change in biogeochemical tracers was negligible. In the model, ligands decay with time (microbial decay). As a result, the addition of hydrothermal ligands does not lead to their unrealistic accumulation in the ocean, with the main anomaly decaying rapidly from the ridge crest (Extended Data Fig. 5). Overall, the addition of hydrothermal ligands in the '1 × Fe + 1 × ligands' and '1 × Fe + 10 × ligands' experiments increases the total ligand inventory from 1.18×10^9 mol to 1.35×10^9 mol. To isolate the effect of hydrothermal ligand supply, we conducted a simulation that added only hydrothermal ligands without hydrothermal Fe_d and compared it to an experiment in which no ligands were added (Extended Data Fig. 5). This experiment is probably not representative of the real ocean, because ligands that might be produced at or near hydrothermal vents would be saturated with the Fe_d supplied by hydrothermal vents. As a consequence this experiment releases ligands into the ocean with an extremely high capacity to complex Fe_d from other sources. In this extreme hypothetical case where unsaturated hydrothermal ligands are able to bind Fe_d from other sources, only a small (~5%) increase in export production in the Southern Ocean is observed.

We have conducted a statistical analysis of the model against the most recent compilation of Fe_d averaged onto the World Ocean Atlas grid. We note that it is challenging to quantitatively evaluate global-scale iron models because we are obliged to compare to localized point measurements rather than having an objective climatology such as those available for macronutrients (for example, World Ocean Atlas). Both the model and the observations were gridded onto 1° × 1° grid with 33 vertical levels. After log-transforming over a depth of 2,000–5,500 m depth, there are 1,025 unique data comparisons. In the abyssal ocean (2,000–5,500 m depth) we find support for the conclusions drawn from the visual model–data comparison in Fig. 4. The correlation (Extended Data Table 1) increases markedly when a source of hydrothermal ligands is applied, relative to the model runs that do not add hydrothermal ligands (1 × Fe and 10 × Fe).

Code availability. The NEMO-PISCES model we use in this work is freely available (<http://www.nemo-ocean.eu/>) under the CeCILL free software licence (<http://www.cecill.info/index.en.html>). We used version 3.4 of the NEMO model and a modified version of the PISCES biogeochemical model. These modifications concern the representation of dynamic ligand cycling and this is not yet present in the freely available NEMO release but will be provided upon contacting A.T.

Hydrothermal plume inventory estimates. Depth-integrated metal inventories for depth intervals of interest were estimated by summing the product of the average concentration of samples from two sequential depths and the difference

in depth between those samples. Where duplicate samples were collected to provide overlap between hydrocast sampling, the average concentration of the samples from overlapping depths was used.

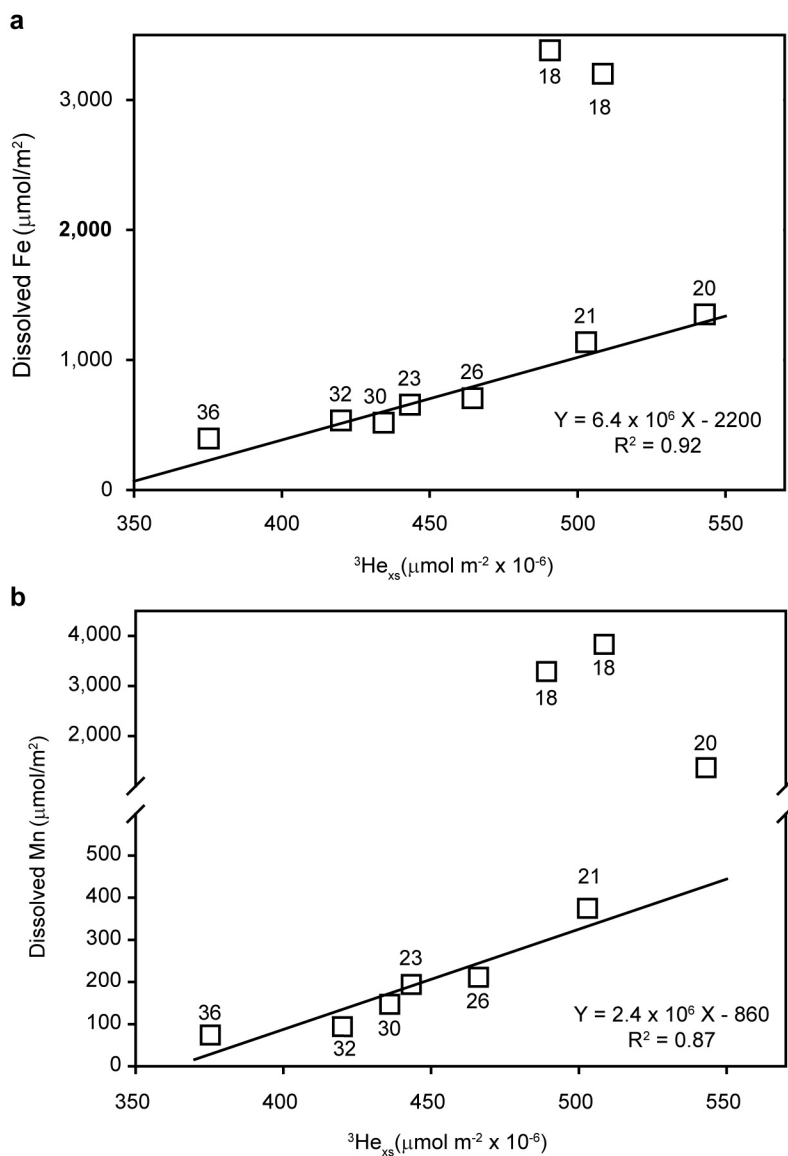
Ocean Data View parameters and adjustments. Ocean Data View (ODV; <http://odv.awi.de/>) was used to produce Fig. 2. ³He_{xs} concentration data were contoured using ODV's Diva gridding algorithm with a signal-to-noise ratio of 10. Dissolved iron concentration data were contoured using the Diva gridding algorithm with a signal-to-noise ratio of 6.5 with negative values suppressed. Dissolved manganese concentration data were contoured using the Diva gridding algorithm with a signal-to-noise ratio of 4 with negative gridded values suppressed. Dissolved aluminium concentration data were contoured using the Diva gridding algorithm with a signal-to-noise ratio of 11 with negative gridded values suppressed.

The extremely high concentrations of these species over the ridge crest (station 18) resulted in interpolated concentrations at station 17 that vastly exceeded the actual measured concentrations. To circumvent this contouring artefact, an artificial background station was inserted at 111.5° W, which is halfway between the ridge-crest station (station 18) and the first station to the east (station 17). This 'background station' duplicated the measured depth and concentration data for each species from station 17. The black sample location indicators for this artificial station were removed from Fig. 2.

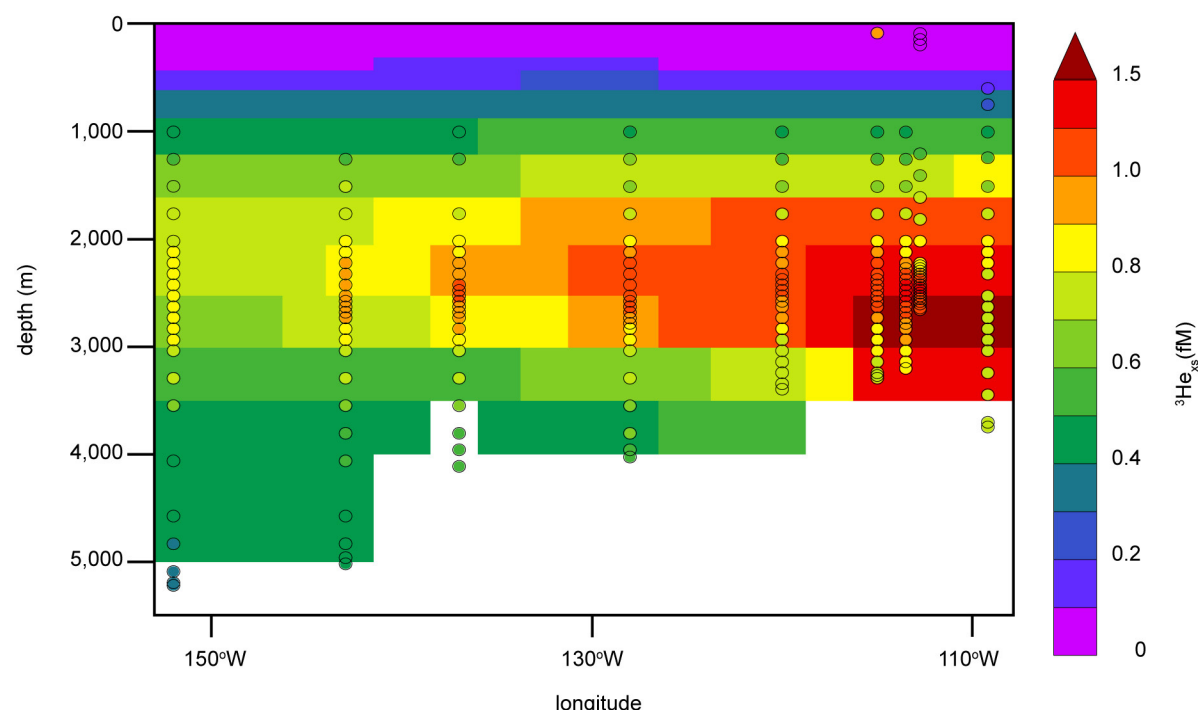
Cruise track selection. The latitude for the western portion of the EPZT cruise was selected to follow the 'downstream' core of the hydrothermal ³He plume close to latitude 15° S, as determined from observations of previous research expeditions in the eastern South Pacific Ocean (the GEOSECS, HELIOS, and WOCE programmes). Urabe *et al.*²⁸ surveyed the SEPR axis between 13.8° S and 18.6° S, finding the most intense hydrothermal plumes between 17° S and 18.5° S. These plumes were rich in particulate iron⁵ and total dissolvable manganese⁵¹. The total dissolvable manganese concentrations at both 2,500 m depth and integrated over 2,200–2,800 m depth in the most intense plumes over the SEPR axis in 1993 were greater than corresponding values observed at any of our EPZT cruise stations. As the ³He data are unpublished, we examine ³He: total dissolvable manganese Mn along the ridge crest²⁸, which has the highest values between 17° S and 18.5° S, suggesting that both discreet and integrated ³He concentrations were much higher in those plumes compared to the plume we sampled at 15° S.

31. Cutter, G. A. & Bruland, K. W. Rapid and noncontaminating sampling system for trace elements in global ocean surveys. *Limnol. Oceanogr. Methods* **10**, 425–436 (2012).
32. Kondo, Y. & Moffett, J. W. Dissolved Fe(II) in the Arabian Sea oxygen minimum zone and western tropical Indian Ocean during the inter-monsoon period. *Deep. Res. I* **73**, 73–83 (2013).
33. Young, C. & Lupton, J. E. An ultratight fluid sampling system using cold-welded copper tubing. *Eos* **64**, 735 (1983).
34. Sedwick, P. N., Bowie, A. R. & Trull, T. W. Dissolved iron in the Australian sector of the Southern Ocean (CLIVAR SR3 section): meridional and seasonal trends. *Deep Sea Res. I* **55**, 911–925 (2008).
35. Sedwick, P. N. *et al.* Iron in the Sargasso Sea (Bermuda Atlantic Time-series Study region) during summer: eddian imprint, spatiotemporal variability, and ecological implications. *Glob. Biogeochem. Cycles* **19**, GB4006 (2005).
36. Measures, C. I., Yuan, J. & Resing, J. A. Determination of iron in seawater by flow injection analysis using in-line preconcentration and spectrophotometric detection. *Mar. Chem.* **50**, 3–12 (1995).
37. Bowie, A. R., Sedwick, P. N. & Worsfold, P. J. Analytical intercomparison between flow injection-chemiluminescence and flow injection-spectrophotometry for the determination of picomolar concentrations of iron in seawater. *Limnol. Oceanogr. Methods* **2**, 42–54 (2004).
38. Resing, J. A. & Mottl, M. J. Determination of manganese in seawater using flow injection analysis with on-line preconcentration and spectrophotometric detection. *Anal. Chem.* **64**, 2682–2687 (1992).
39. Resing, J. & Measures, C. Fluorometric determination of Al in seawater by flow injection analysis with in-line preconcentration. *Anal. Chem.* **66**, 4105–4111 (1994).
40. Moffett, J. W., Goepfert, T. G. & Naqvi, S. W. A. Reduced iron associated with secondary nitrite maxima in the Arabian Sea. *Deep Sea Res. I* **54**, 1341–1349 (2007).
41. Stanley, R. H. R., Baschek, B., Lott, D. E. & Jenkins, W. J. A new automated method for measuring noble gases and their isotopic ratios in water samples. *Geochem. Geophys. Geosyst.* **10**, Q05008 (2009).
42. Lott, D. E. Improvements in noble gas separation methodology: a nude cryogenic trap. *Geochem. Geophys. Geosyst.* **2**, 2001GC000202 (2001).
43. Lott, D. & Jenkins, W. J. An automated cryogenic charcoal trap system for helium isotope mass spectrometry. *Rev. Sci. Instrum.* **55**, 1982–1988 (1984).
44. Benson, B. B. & Krause, D. J. Isotopic fractionation of helium during solution: a probe for the liquid state. *J. Solution Chem.* **9**, 895–909 (1980).
45. Völker, B. M. & Tagliabue, A. Modeling organic iron-binding ligands in a three-dimensional biogeochemical ocean model. *Mar. Chem.* **173**, 67–77 (2015).
46. Aumont, O. & Bopp, L. Globalizing results from ocean in situ iron fertilization studies. *Glob. Biogeochem. Cycles* **20**, GB2017 (2006).

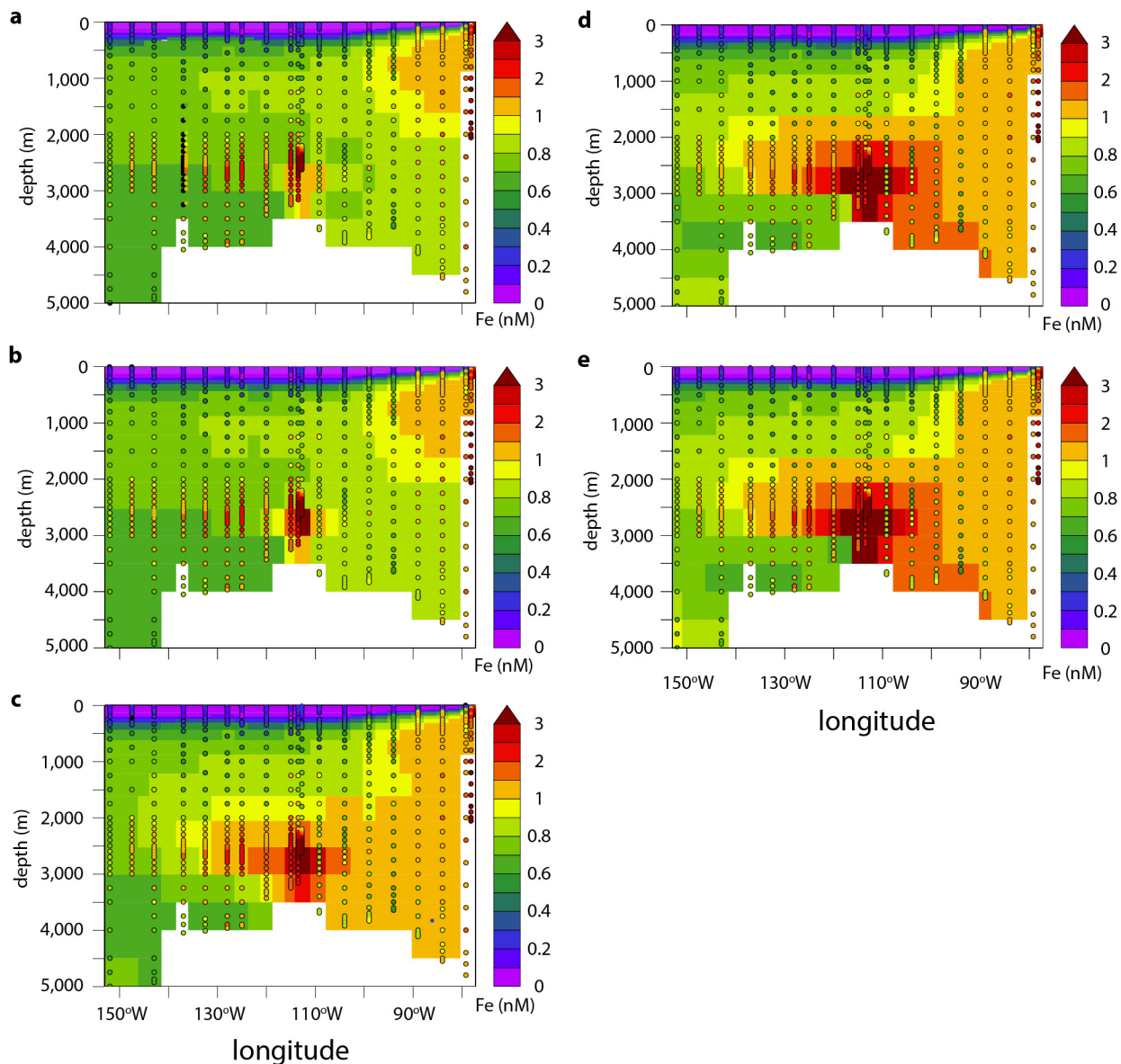
47. Tagliabue, A., Aumont, O. & Bopp, L. The impact of different external sources of iron on the global carbon cycle. *Geophys. Res. Lett.* **41**, 920–926 (2014).
48. Liu, X. & Millero, F. J. The solubility of iron in seawater. *Mar. Chem.* **77**, 43–54 (2002).
49. Liu, X. & Millero, F. J. The solubility of iron hydroxide in sodium chloride solutions. *Geochim. Cosmochim. Acta* **63**, 3487–3497 (1999).
50. Flynn, K. & Hipkin, C. Interactions between iron, light, ammonium, and nitrate: insights from the construction of a dynamic model of algal physiology. *J. Phycol.* **35**, 1171–1190 (1999).
51. Ishibashi, J. et al. Hydrothermal methane and manganese variation in the plume over the superfast-spreading southern East Pacific Rise. *Geochim. Cosmochim. Acta* **61**, 485–500 (1997).



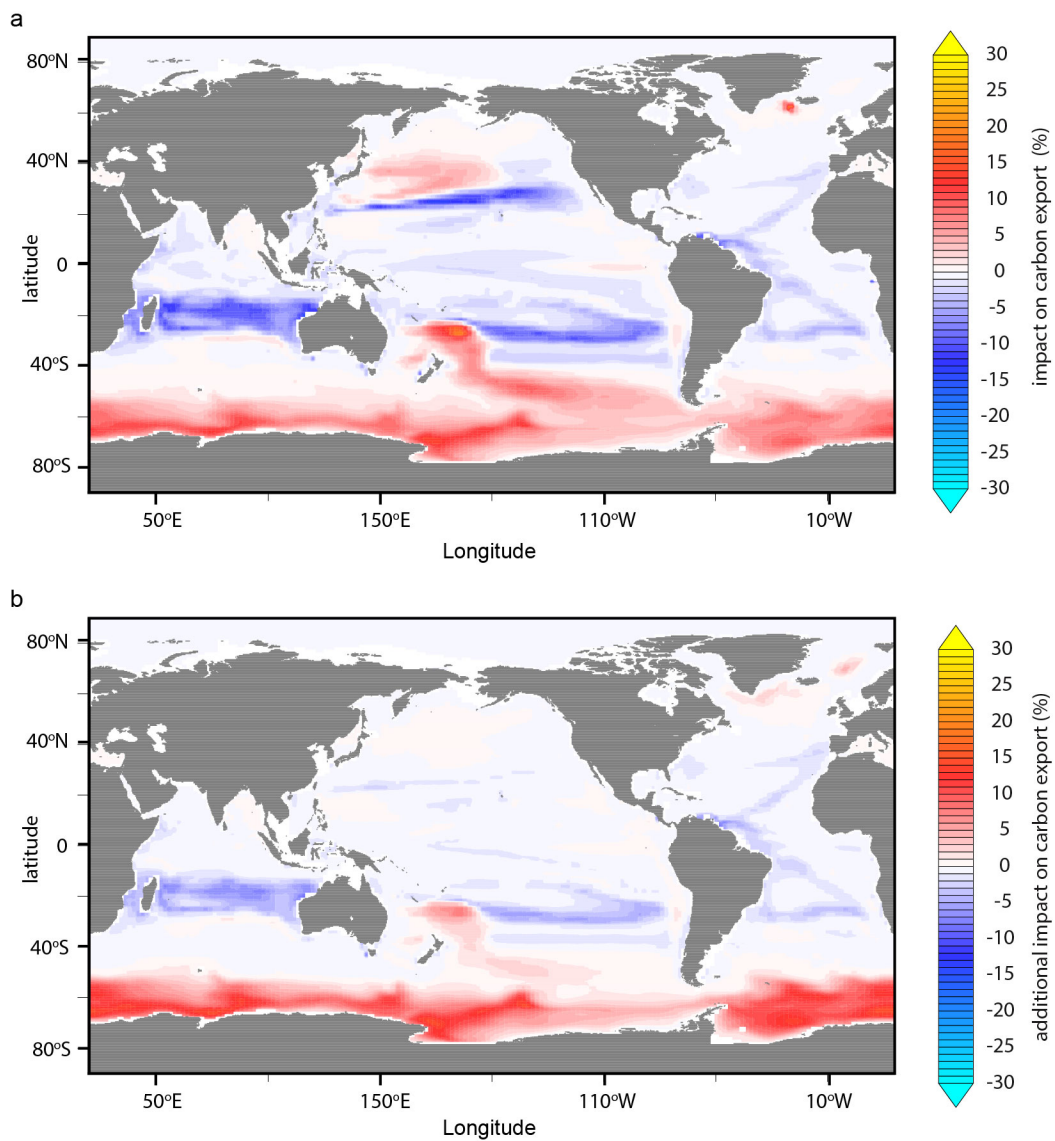
Extended Data Figure 1 | Relationship between dissolved trace metals and ${}^3\text{HE}$. Depth-integrated concentrations of dissolved Fe (a), and dissolved Mn (b), versus depth-integrated concentration of ${}^3\text{He}_{xs}$, over a depth range of 2,200–2,640 m. Sample station numbers are indicated for each data symbol.



Extended Data Figure 2 | Comparison of modelled (rectangles) and measured (circular symbols) concentrations of ${}^3\text{He}_{\text{xs}}$ between EPZT cruise station 36 (far left) and station 17 (far right).

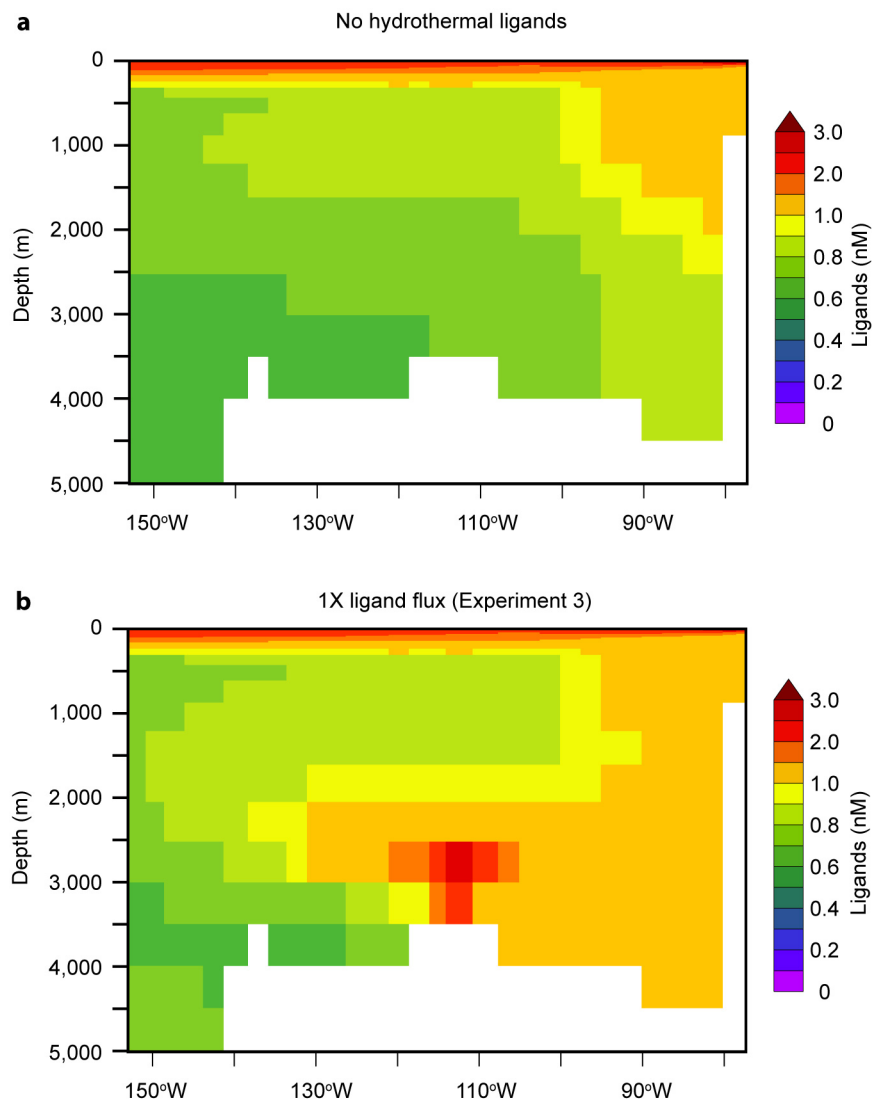


Extended Data Figure 3 | Sections of modelled Fe_d transport and decay using a dynamic ligand global-circulation model⁴⁵ (see Methods). The model scenarios listed here are the same as those presented in Fig. 4. **a**, $1 \times \text{Fe}$; **b**, $10 \times \text{Fe}$; **c**, $1 \times \text{Fe} + 1 \times \text{ligands}$; **d**, $1 \times \text{Fe} + 10 \times \text{ligands}$; **e**, $10 \times \text{Fe} + 10 \times \text{ligands}$.


Extended Data Figure 4 | Impacts on carbon export from model

simulations. **a**, Percentage contribution to carbon export production due to the input of hydrothermal Fe_d , not considering the addition of hydrothermal ligands. **b**, Additional percentage contribution from the addition of

hydrothermal ligands to the simulation shown in **a**. **b** represents the difference between the total impact from the addition of both hydrothermal Fe_d and ligands (see Fig. 4c) compared to the input hydrothermal Fe_d without the addition of the ligands shown in **a**.



Extended Data Figure 5 | Ligand flux model experiments. Two experiments were run to assess the impact of the flux of ligands associated with hydrothermal activity on the oceanic budget. **a**, Model simulation with no hydrothermal ligand flux. **b**, Model simulation with ligand flux equal to the flux of hydrothermal Fe.

Extended Data Table 1 | Model data comparison

		R	Mean Fe _d (nM)
Model scenarios	1 x Fe	0.12	0.59
	10 x Fe	0.30	0.61
	1 x Fe + 1 x ligands	0.42	0.71
	1 x Fe + 10 x ligands	0.47	0.87
	10 x Fe + 10 x ligands	0.59	1.02
Measurements	-	-	0.66

Comparisons between log-transformed model output and measurements of Fe_d averaged over the World Ocean Atlas grid (1° × 1° with 33 vertical levels) resulted in 1,025 individual model-data pairs at 2,000–5,500 m depth. R is the correlation between the modelled output and measurements.

Copyright of Nature is the property of Nature Publishing Group and its content may not be copied or emailed to multiple sites or posted to a listserv without the copyright holder's express written permission. However, users may print, download, or email articles for individual use.